

# Journal of Materials Chemistry A

Accepted Manuscript



This is an *Accepted Manuscript*, which has been through the Royal Society of Chemistry peer review process and has been accepted for publication.

*Accepted Manuscripts* are published online shortly after acceptance, before technical editing, formatting and proof reading. Using this free service, authors can make their results available to the community, in citable form, before we publish the edited article. We will replace this *Accepted Manuscript* with the edited and formatted *Advance Article* as soon as it is available.

You can find more information about *Accepted Manuscripts* in the [Information for Authors](#).

Please note that technical editing may introduce minor changes to the text and/or graphics, which may alter content. The journal's standard [Terms & Conditions](#) and the [Ethical guidelines](#) still apply. In no event shall the Royal Society of Chemistry be held responsible for any errors or omissions in this *Accepted Manuscript* or any consequences arising from the use of any information it contains.

# Quantitative investigation on hydrogenation to the performance of MnO<sub>2</sub>/H-TiO<sub>2</sub> composite electrodes for supercapacitor

X. Y. Cao,<sup>a</sup> X. Xing,<sup>c</sup> N. Zhang,<sup>b</sup> H. Gao,<sup>a</sup> M. Y. Zhang,<sup>\*,a</sup> and Y. C. Shang,<sup>c</sup> X. T. Zhang.<sup>\*,a</sup>

<sup>a</sup> Key Laboratory for Photonic and Electronic Bandgap Materials, Ministry of Education, School of Physics and Electronic Engineering, Harbin Normal University, Harbin 150025, P. R. China.

<sup>b</sup> Department of Chemistry and Chemical Biology, Cornell University, Ithaca, USA.

<sup>c</sup> College of Chemistry and Chemical Engineering, Harbin Normal University, Harbin 150025, P. R. China.

In this paper, the high-performance MnO<sub>2</sub>/H-TiO<sub>2</sub>/carbon-microfiber nanowire composite electrodes were successfully synthesized. Their crystalline properties and electrical conductivity of H-TiO<sub>2</sub> nanowires were studied by X-ray diffraction, Raman scattering and Mott-Schottky theory. In order to quantitatively investigate the contribution of hydrogenation to the performance of MnO<sub>2</sub>/H-TiO<sub>2</sub> composite electrodes, their electrochemical performance and electrochemical impedance spectroscopy were quantitatively investigated, respectively. The physical mechanism is proposed based on the theory of semiconductor physics. Typically, for the hydrogenated composite electrode at 600 °C, the specific capacitance reaches 630.1 F g<sup>-1</sup> at 10 mV s<sup>-1</sup> and the high energy density of 46.0 Wh kg<sup>-1</sup> is obtained at the high power density of 21.8 kW kg<sup>-1</sup>. Moreover, the

---

\*Corresponding author emails: [zhangmingyi@hrbnu.edu.cn](mailto:zhangmingyi@hrbnu.edu.cn), [xtzhangzhang@hotmail.com](mailto:xtzhangzhang@hotmail.com)

capacitance retention is 90% after 5000 cycles. This work provides an idea for rationally designing the high-performance supercapacitors and assembling novel nanostructures with preferable electrochemical performance.

## 1. Introduction

The sustainable and renewable energy resources have been developed to meet the increasing energy demands for the myriad applications from portable consumer electronic devices to electrical vehicles, and reduce the environmental pollution.<sup>1-3</sup> Energy storage system for advanced power applications are an important part of power generation systems. Among them, supercapacitors (SCs) have been considered as a very promising candidate due to their high power density, fast charging/discharging rate, high energy density and excellent cycling stability in recent years.<sup>4-6</sup> SCs are usually grouped into two categories: electrical double-layer capacitors (EDLCs) and pseudocapacitors (PCs) on the basis of the charge storage mechanism.<sup>5-8</sup> Compared with EDLCs, which store charges by electrostatic charge diffusion and accumulation at the electrode/electrolyte interfaces, PCs exhibit much higher specific capacitance and energy density through fast and reversible surface or near-surface redox reactions for charge storage.<sup>4</sup> Therefore, most of recent studies on PCs have been focused on the development of redox-active materials with high specific capacitance and good stability.<sup>9-16</sup>

Recently, transition metal oxides, such as  $\text{RuO}_2$ ,<sup>9</sup>  $\text{NiO}$ ,<sup>10</sup>  $\text{Co}_3\text{O}_4$ ,<sup>11,12</sup>  $\text{V}_2\text{O}_5$ ,<sup>13</sup>  $\text{TiO}_2$ <sup>14,15</sup> and  $\text{MnO}_2$ ,<sup>16,17</sup> are considered to be potential electrode materials for PCs. Among them,  $\text{MnO}_2$  could be one of the most attractive materials for PCs due to its outstanding characteristics, such as high theoretical specific capacitance ( $\sim 1370 \text{ F g}^{-1}$ ), wide operating potential window in mild

electrolyte, low cost, natural abundance, and environmental friendliness.<sup>1</sup> However, it is the poor electric conductivity ( $10^{-5}$ – $10^{-6}$  S cm<sup>-1</sup>) that gives rise to the deviation of its specific capacitance from high theoretical value in experiments.<sup>18-20</sup> In order to overcome the drawback, great effort has been taken. For instance, the electrochemical properties of Zn<sub>2</sub>SnO<sub>4</sub>/MnO<sub>2</sub>,<sup>6</sup> Co<sub>3</sub>O<sub>4</sub>@MnO<sub>2</sub>,<sup>18</sup> carbon nanoparticles/MnO<sub>2</sub> nanorods,<sup>19</sup> MnO<sub>2</sub>-shell/ZnO-nanowire,<sup>21</sup> and SnO<sub>2</sub>/MnO<sub>2</sub><sup>22</sup> were studied, respectively. The MnO<sub>2</sub> compositing with other nanostructures has recently become one of the basic approaches in designing high-performance electrodes for MnO<sub>2</sub>-based PCs.

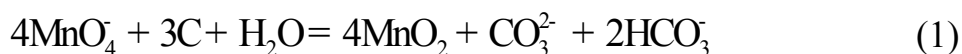
It is well known that TiO<sub>2</sub> is abundant, low cost and environmental benign with stable chemical nature, so it has been widely studied in many domains, especially in electrochemical devices. Furthermore, it has the higher electrical conductivity ( $10^{-5}$ – $10^{-2}$  S cm<sup>-1</sup>) than MnO<sub>2</sub>.<sup>23-25</sup> In particular, hydrogenation can greatly improve electrical conductivity of TiO<sub>2</sub>.<sup>23,25</sup> Hence, it will be an excellent strategy that the hydrogenated TiO<sub>2</sub> (H-TiO<sub>2</sub>) is applied as the core for the MnO<sub>2</sub> shell. Recently, H-TiO<sub>2</sub>@MnO<sub>2</sub> (hydrogenated at 800 °C) reported by Lu et al. yielded high specific capacitance of 449.6 F g<sup>-1</sup>, much higher than TiO<sub>2</sub>@MnO<sub>2</sub> (359.7 F g<sup>-1</sup>) and MnO<sub>2</sub> (325.8 F g<sup>-1</sup>) at the scan rate of 10 mV s<sup>-1</sup>.<sup>26</sup> However, the physical mechanism for the increase of electric conductivity in TiO<sub>2</sub> via hydrogenation is rarely reported.<sup>26,27</sup> It is essential to understand the mechanism in order to design a high performance SC and assemble novel nanostructures with preferable electrochemical performance.

In this work, we synthesized an ultrathin layer (about 5 nm) of  $\text{MnO}_2$  coated on the H- $\text{TiO}_2$  nanowires (NWs) grown on flexible carbon microfibers (labeled as  $\text{MnO}_2/\text{H-TiO}_2/\text{CMF}$  NWs), and then quantitatively studied the effect of the hydrogenated temperature varying from 400 °C to 800 °C on the electrochemical performance of  $\text{MnO}_2/\text{H-TiO}_2/\text{CMF}$  NW composite electrodes. The hydrogenated composite electrode at 600 °C exhibits the highest specific capacitance, energy density, power density, and excellent cycling stability. Such results are well explained and the physical mechanism of the improving electrical conductivity by hydrogenation is proposed in terms of the theory of semiconductor physics.

## 2. Experimental Section

**Materials Synthesis:** All of the reagents used in the experiment were of analytical grade without further purification. Prior to the synthesis, the CMF substrate (WOS1002, 2.5 cm x 1.0 cm x 360  $\mu\text{m}$ ) was cleaned by ultrasonication in acetone, ethanol, and deionized water for 30 min in turn, respectively. Firstly,  $\text{TiO}_2$  NWs were directly grown on the CMF substrate by a seed-assisted hydrothermal method (for details, see the Experimental Section of Supporting Information). Then, the as-synthesized  $\text{TiO}_2/\text{CMF}$  NWs were annealed in hydrogen atmosphere at 400 °C, 600 °C, and 800 °C for 1 h, respectively. The process of thermal treatment was performed in a continuous fixed bed reactor system filled with ultrahigh purity hydrogen gas, and the flow rate of hydrogen was 17 mL/min. Secondly, the H- $\text{TiO}_2/\text{CMF}$  NWs were used as the scaffold for the ultrathin  $\text{MnO}_2$  shell layer.

0.035 M glucose aqueous solution with H-TiO<sub>2</sub>/CMF NWs was transferred to a 40 mL Teflon-lined stainless steel autoclave, and then the autoclave was maintained at 180 °C for 3 h. A layer of carbon formed on the surface of H-TiO<sub>2</sub>/CMF NWs to be used as a sacrificial layer for the reduction of KMnO<sub>4</sub> to form MnO<sub>2</sub> via the following reaction at room temperature,<sup>28,29</sup>



That is, 0.05 M KMnO<sub>4</sub> and 0.05 M Na<sub>2</sub>SO<sub>4</sub> were mixed with equal volume, and then the samples were immersed in the mixture for 4 h at room temperature. In addition, the MnO<sub>2</sub> nanostructures were directly coated on the surface of CMFs by the similar method above.

**Materials Characterization:** The morphology and the structure of the electrodes were characterized by field emission scanning electron microscopy (FE-SEM; SU70, Hitachi, Japan), transmission electron microscopy (TEM; FEI, Tecnai TF20) with an energy-dispersive X-ray spectroscopy (EDS) and X-ray diffraction (XRD; D/max2600, Rigaku, Japan) using the Cu K $\alpha$  radiation ( $\lambda = 1.5418 \text{ \AA}$ ), respectively. Raman spectra were measured by Micro-Raman spectrometer (J-Y, HR800, France) at a wavelength of 488 nm as the excitation source.

**Electrochemical Measurements:** Electrochemical measurements were conducted in an electrochemical workstation (VMP3, France) with a standard three-electrode electrochemical cell. The MnO<sub>2</sub>/TiO<sub>2</sub>/CMF NW composite electrode, MnO<sub>2</sub>/H-TiO<sub>2</sub>/CMF NW composite electrode, TiO<sub>2</sub>/CMF NW electrode, and MnO<sub>2</sub>/CMF electrode were directly used as

the freestanding working electrode, respectively. The Pt foil and the standard calomel electrode (SCE) were used as the counter electrode and the reference electrode, respectively. The electrochemical performance of the as-synthesized electrodes was studied by means of the cyclic voltammetry (CV) and galvanostatic charging/discharging (GCD) techniques with the potential window from 0 V to 1.0 V. Moreover, the electrochemical impedance spectroscopy (EIS) measurements were performed by applying an alternating-current voltage with 5 mV amplitude in a frequency range from 0.01 Hz to 100 kHz. And Mott-Schottky (M-S) plots were measured at the frequency of 10 Hz. All measurements were carried out in 0.5 M Na<sub>2</sub>SO<sub>4</sub> electrolyte at room temperature.

### 3. Results and Discussions

The morphology of H-TiO<sub>2</sub>/CMF NWs at 600 °C was studied by SEM, as shown in Figure 1(a). The quasi-aligned H-TiO<sub>2</sub> NWs are radially and uniformly grown on the surface of CMFs. Figure 1(b) demonstrates a corresponding high-magnified SEM image of H-TiO<sub>2</sub>/CMF NWs from Figure 1(a). The diameters of H-TiO<sub>2</sub> NWs are 25-65 nm and their lengths are about 1.2 μm. Moreover, the obtained H-TiO<sub>2</sub> NWs have perfect tetragonal cross-sections and relatively smooth surfaces. The H-TiO<sub>2</sub> NWs are used as the scaffold for the ultrathin coating of amorphous MnO<sub>2</sub>. Figure 1(c) shows a low-magnified SEM image of the MnO<sub>2</sub>/H-TiO<sub>2</sub>/CMF composite NWs at 600 °C. The morphology of the NWs still remains unchanged after deposition of the MnO<sub>2</sub> layer onto the H-TiO<sub>2</sub> NWs. Figure

1(d) shows a magnified SEM image of the local area in the Figure 1(c). It is worth noting that the surfaces of the NWs turn to rough, indicating the formation of  $\text{MnO}_2$  shell on the surface of H- $\text{TiO}_2$  NWs. In addition, the morphologies of  $\text{TiO}_2/\text{CMF}$  NWs and H- $\text{TiO}_2/\text{CMF}$  NWs at 400 °C and 800 °C are similar to these (Figure S1). In other words, the effect of hydrogenation on the morphology of  $\text{TiO}_2/\text{CMF}$  NWs is negligible.

The morphology and microstructure of the  $\text{MnO}_2/\text{H-TiO}_2/\text{CMF}$  composite NWs at 600 °C were further studied by TEM. Figure 2(a) shows a TEM image of a bare H- $\text{TiO}_2$  NW with a smooth surface. Figure 2(b) clearly reveals the core/shell structure of a  $\text{MnO}_2/\text{H-TiO}_2$  NW. The rough and bright thin layer on the surface of the NW originates from the  $\text{MnO}_2$  layer. The corresponding selected area electron diffraction pattern is shown in Figure 2(c). From the figure 2(c), the regular diffraction pattern belonging to the tetragonal  $\text{TiO}_2$  indicates that the H- $\text{TiO}_2$  NW is a single crystalline and grows along the [001] direction, while diffuse halo rings in the figure 2(c) indicate that  $\text{MnO}_2$  is amorphous. These results can be further confirmed by high-resolution TEM observation, as shown in Figure 2(d). The regular and random atom arrangements demonstrate the crystalline state of H- $\text{TiO}_2$  and amorphous state of  $\text{MnO}_2$  once again, respectively. The lattice spacing of 0.32 nm (the inset of Figure 2(d)) is in good agreement with the d-spacing of (110) plane of rutile  $\text{TiO}_2$ . What's more, it can be seen that an ultrathin layer of  $\text{MnO}_2$  with an average thickness of 5 nm is uniformly coated on the surface of the H- $\text{TiO}_2$  NWs, revealing the formation of the core/shell

architecture clearly. The elemental spatial distributions of the compositional elements within the  $\text{MnO}_2/\text{H-TiO}_2$  NW were characterized by the EDS line-scanning (indicated by the red line in the inset) along the radial direction of the NW. There are three signal peaks in Ti, Mn, and O, as shown in Figure 2(e). The Ti signal is mainly confined within the  $\text{TiO}_2$  core area, while the Mn signal is found in the shell. The O signal appears within the core and the shell. This confirms the core/shell structure of the  $\text{MnO}_2/\text{TiO}_2$  NW again. Analysis of the data shows that the diameters of the  $\text{TiO}_2$  NW and the composite NW are about 55 nm and 65 nm, respectively, consistent with the high-resolution TEM image (Figure 2(d)). The core/shell architecture has the capability to improve the electrochemical performance of the composite electrodes, as proved below.

The crystallographic structures and the possible phase changes of the  $\text{TiO}_2$  NWs during hydrogenation from 400 °C to 800 °C were investigated by XRD. Figure 3(a) shows XRD patterns of the untreated  $\text{TiO}_2/\text{CMF}$  NWs and  $\text{H-TiO}_2/\text{CMF}$  NWs at different temperatures. From the XRD patterns, all peaks for each sample can be readily indexed to rutile  $\text{TiO}_2$  (JCPDF No. 77-0442) except the peaks centered at 25.6° and 42.9° from CMF substrate. Thus, there is no phase change during hydrogenation. In order to quantitatively study the effect of the hydrogenated temperature on the electrochemical performance of the composite electrodes, the full width at half maximums (FWHMs) of the diffraction peaks for the untreated  $\text{TiO}_2/\text{CMF}$  NWs and the  $\text{H-TiO}_2/\text{CMF}$  NWs at different temperatures are

listed in Table I. From Table I, the FWHM gradually becomes narrow with the hydrogenated temperature rising. Especially, the FWHM obviously becomes narrow when the temperature reaches as high as 800 °C. The obvious improvement of the crystalline quality indicates the rapid reduction of the intrinsic defects (or oxygen vacancies) of the H-TiO<sub>2</sub> NWs at 800 °C, suggesting that electrical conductivity should be affected due to the change of the electron concentration.

The possible changes of TiO<sub>2</sub> NWs on the structure and phase during hydrogenation were further studied by Raman spectra. From Figure 3(b), the typical Raman peaks of untreated TiO<sub>2</sub> NWs appear at 145 cm<sup>-1</sup>, 240 cm<sup>-1</sup>, 446 cm<sup>-1</sup>, and 609 cm<sup>-1</sup>, which can be ascribed to the B<sub>1g</sub>, two-phonon scattering (TPS), E<sub>g</sub>, and A<sub>1g</sub> modes of rutile TiO<sub>2</sub>, respectively.<sup>30,31</sup> Compared with untreated TiO<sub>2</sub> NWs, Raman peak positions of H-TiO<sub>2</sub> NWs show an obvious red-shift, and their red-shift becomes large for the H-TiO<sub>2</sub> NWs at 400 °C, 800 °C, and 600 °C in sequence, especially to the E<sub>g</sub> mode which is more sensitive. It is reported that the phonon confinement<sup>32</sup> and the oxygen stoichiometry<sup>33</sup> can contribute to the change of the peak position for rutile TiO<sub>2</sub>. The red-shift results mainly come from the phonon confinement when the size of crystalline grain is smaller than 10 nm. Otherwise, it could be from the oxygen stoichiometry. From our TEM data, the diameters of TiO<sub>2</sub> NWs are larger than 20 nm and the possibility of size confinement effects is ruled out. From XRD analysis, the intrinsic defects reduce slightly with the hydrogenation temperature rising, and to 800 °C, the intrinsic

defects greatly reduce, i.e., the crystalline quality of the TiO<sub>2</sub> NWs is significantly improved. Thus, the red-shift of the Raman peak contradicts the reduction of the intrinsic defects. We propose that the incorporation of the hydrogen atoms into the TiO<sub>2</sub> NWs could play an important role in the red-shift except the intrinsic defects. During hydrogenation, hydrogen atoms doped into TiO<sub>2</sub> could occupy the substitutional sites or the interstitial sites to form hydrogen defects (H<sub>O</sub> or H<sub>i</sub>) or hydroxide defects (HO<sub>o</sub><sup>-</sup>) (see below). They could behave as shallow donor centers in TiO<sub>2</sub>. These defects would change their local lattice fields, which would result in the change of the lattice vibration frequency. Thus the incorporation of the hydrogen atoms plays an important role in the red-shift.

To study the electrochemical performance of the as-synthesized MnO<sub>2</sub>/TiO<sub>2</sub>/CMF NW composite electrode, the electrochemical measurements were conducted in a three-electrode electrochemical cell with the potential window from 0 V to 1.0 V versus (vs.) SCE in 0.5 M Na<sub>2</sub>SO<sub>4</sub> aqueous solution. Figure 4(a) shows the CV curve of the MnO<sub>2</sub>/TiO<sub>2</sub>/CMF NW composite electrode at the scan rate of 10 mV s<sup>-1</sup>. No peaks are observed, indicating that the electrode is charged and discharged at a pseudo-constant rate over the complete voltammetric cycle. The CV curve shows a symmetric quasi-rectangular shape. In order to demonstrate that the electrochemical performance benefits from the MnO<sub>2</sub>/TiO<sub>2</sub>/CMF NW composite electrode, CV tests of the TiO<sub>2</sub>/CMF NW electrode and MnO<sub>2</sub>/CMF electrode were carried out at the same scan rate of 10 mV s<sup>-1</sup>, as

shown in Figure 4(a). The measured CV curves also show quasi-rectangular shapes. However, the separation between the charged and discharged curve for the TiO<sub>2</sub>/CMF NW electrode is much smaller than that of the MnO<sub>2</sub>/TiO<sub>2</sub>/CMF NW composite electrode, revealing that the contribution of the TiO<sub>2</sub>/CMF is negligible. The specific capacitance of the electrodes is calculated according to the following equation (Eq.) (2),

$$C = \frac{\int i \, dV}{m \cdot v \cdot \Delta U} \quad (2)$$

where  $C$  (F g<sup>-1</sup>),  $m$  (g),  $v$  (mV s<sup>-1</sup>),  $\Delta U$  (V), and  $i$  (A) are specific capacitance, the mass of active materials, the potential scan rate, the potential window, and the voltammetric current, respectively. Here the loading mass of the MnO<sub>2</sub> is 0.27±0.01 mg/cm<sup>2</sup>. The specific capacitance of the MnO<sub>2</sub>/TiO<sub>2</sub>/CMF NW composite electrode is 299.1 F g<sup>-1</sup>, while those of MnO<sub>2</sub>/CMF electrode and TiO<sub>2</sub>/CMF NW electrode only achieve 100.3 F g<sup>-1</sup> and 5.2 F g<sup>-1</sup>, respectively. The capacitance of the composite electrode is much larger than the MnO<sub>2</sub>/CMF electrode, proving the superiority of the core/shell architecture. This should be attributed to increasing the active sites and improving the charge transport in the composite NWs. The analogous results are also obtained from GCD curves (Figure 4(b)). The longest discharge time of the composite electrode indicates its best electrochemical performance. To further clarify the role of CMF, we studied the electrochemical performance of CMF substrate for freestanding electrode, as shown in Figure S2. From it, the CMF can hardly contribute the capacitance

for the composite electrode (for details, see the Supporting Information). Thus the CMF substrate with excellent electrical conductivity only acts as the current collector in the composite electrode. The CV measurements of the MnO<sub>2</sub>/TiO<sub>2</sub>/CMF NW composite electrode were conducted at different scan rates, as shown in Figure 4(c). All CV curves exhibit symmetric quasi-rectangular shapes, indicating the ideal pseudo-capacitive behavior with highly reversibility at each scan rate. Figure 4(d) shows the GCD curves with very symmetric triangular shapes, revealing the good pseudo-capacitive behavior and a highly reversible Faradic reaction at different current densities as well.

In order to quantitatively investigate the effect of the hydrogenated temperature on the electrochemical performance of the MnO<sub>2</sub>/TiO<sub>2</sub>/CMF NW composite electrode, the CV and GCD measurements of the MnO<sub>2</sub>/H-TiO<sub>2</sub>/CMF NW composite electrodes at different temperatures from 400 °C to 800 °C were carried out, respectively. Figure 5(a) shows the CV curves of the hydrogenated composite electrodes at the scan rate of 10 mV s<sup>-1</sup>. The capacitive current density of the MnO<sub>2</sub>/H-TiO<sub>2</sub>/CMF NW composite electrodes significantly increases with the hydrogenated temperature rising, and it reaches the highest at 600 °C. The value of the specific capacitance reaches as high as 536.6 F g<sup>-1</sup> at 10 mV s<sup>-1</sup>, while those of the hydrogenated composite electrodes at 800 °C and 400 °C are 447.9 F g<sup>-1</sup> and 381.6 F g<sup>-1</sup>, respectively, and that of the untreated composite electrode is only 299.1 F g<sup>-1</sup>. All the CV curves (Figure S3) of the MnO<sub>2</sub>/H-TiO<sub>2</sub>/CMF NW composite

electrodes at different temperatures at various scan rates exhibit symmetric quasi-rectangular shapes, indicating the good capacitive performance, similar to those of the MnO<sub>2</sub>/TiO<sub>2</sub>/CMF NW composite electrode. Note that it can be observed that the current responses at high and low potentials are deviated from the equilibrium state due to the electrochemical polarization occurring, especially at high scan rate. This irreversible polarization may accelerate the reduction of MnO<sub>2</sub> to soluble Mn<sup>2+</sup> and thus result in rapid capacitance degradation. And the ions in the electrolyte can't diffuse sufficiently into the interior surfaces to participate in the reactions for more charge storage at high scan rate. So the specific capacitance fades with the increase of the scan rate, as shown in Figure 5(b). The specific capacitance of each composite electrode as a function of the scan rate is plotted in Figure 5(b). Remarkably, the error bars in Figure 5 mainly originate from the mass accuracy of the ultrathin MnO<sub>2</sub> layer. It can be seen that the specific capacitance of the MnO<sub>2</sub>/H-TiO<sub>2</sub>/CMF NW composite electrode at 600 °C is higher than others at each scan rate within the error and it is the best among the capacitance retentions of the different hydrogenated composite electrodes.

Rate capability is an important factor for evaluating the power application of SCs. The GCD curves of the MnO<sub>2</sub>/H-TiO<sub>2</sub>/CMF NW composite electrodes at various current densities are shown in Figure S3. Both the linear profile of charge/discharge curves and their symmetry reveal the good capacitive feature and superior reversible redox reactions once again. Notably, the low

voltage loss (also called IR drop) exhibits the low internal resistance even at high current density, indicating the good performance. The different charging/discharging time and IR drop result in the different specific capacitance, and the difference can be qualitatively observed from the GCD curves of the different composite electrodes at the current density of  $10 \text{ A g}^{-1}$ , as shown in Figure 5(c). Among them, the discharging time (50.5 s) of the  $\text{MnO}_2/\text{H-TiO}_2/\text{CMF}$  NW composite electrode at  $600 \text{ }^\circ\text{C}$  is the longest, and its IR drop (0.025 V) is also the smallest. Its specific capacitance is  $518.2 \text{ F g}^{-1}$  at  $10 \text{ A g}^{-1}$ , according to the following Eq. (3),

$$C = \frac{I \times \Delta t}{m \times \Delta U} \quad (3)$$

where  $C$  ( $\text{F g}^{-1}$ ),  $m$  (g),  $\Delta U$  (V),  $I$  (A), and  $t$  (s) are specific capacitance, the mass of active materials, the actual potential window in the discharging process, the applied current, and the discharging time, respectively. It agrees well with the results of the CV tests. From Figure 5(d), the specific capacitance of the  $\text{MnO}_2/\text{H-TiO}_2/\text{CMF}$  NW composite electrodes at  $600 \text{ }^\circ\text{C}$ ,  $800 \text{ }^\circ\text{C}$ ,  $400 \text{ }^\circ\text{C}$ , and  $\text{MnO}_2/\text{TiO}_2/\text{CMF}$  NW composite electrode is reduced in sequence at each current density within the error. The value of IR drop for the hydrogenated composite electrodes at  $600 \text{ }^\circ\text{C}$  (0.025 V),  $800 \text{ }^\circ\text{C}$  (0.034 V),  $400 \text{ }^\circ\text{C}$  (0.036 V) and the untreated composite electrode (0.046 V) at  $10 \text{ A g}^{-1}$  can be served as a proof for the non-linearly improving performance with the hydrogenated temperature rising. Furthermore, the capacitance decreases for each composite electrode with the increase of the current density, as shown in Figure 5(d). When the current density changes from  $1 \text{ A}$

$\text{g}^{-1}$  to  $100 \text{ A g}^{-1}$ , the capacitance retention of the  $\text{MnO}_2/\text{H-TiO}_2/\text{CMF}$  NW composite electrode at  $600 \text{ }^\circ\text{C}$  is about 59%, which is higher than that of others (56%, 53%, and 33% for the hydrogenated composite electrodes at  $800 \text{ }^\circ\text{C}$ ,  $400 \text{ }^\circ\text{C}$ , and the untreated composite electrode, respectively). The best rate capability of the  $\text{MnO}_2/\text{H-TiO}_2/\text{CMF}$  NW composite electrode at  $600 \text{ }^\circ\text{C}$  can be attributed to the relatively better conductivity, indicating the promising application.

Energy density and power density are two key parameters for evaluating the performance of SCs. The excellent performance is expected to exhibit high energy density with high power density. Figure 5(e) shows the Ragone plots of the different composite electrodes. As can be seen, the  $\text{MnO}_2/\text{H-TiO}_2/\text{CMF}$  NW composite electrode at  $600 \text{ }^\circ\text{C}$  also exhibits the highest energy density and the highest power density among different electrodes. The energy density and power density of the electrodes can be calculated from the following Eqs. (4) and (5) in GCD, respectively,

$$E = \frac{1}{2}CU^2 \quad (4)$$

$$P = E/t \quad (5)$$

where  $E$  ( $\text{Wh kg}^{-1}$ ),  $P$  ( $\text{kW kg}^{-1}$ ),  $C$  ( $\text{F g}^{-1}$ ),  $U$  (V), and  $t$  (s) are energy density, power density, specific capacitance, the actual potential window in discharging process, and the discharge time, respectively. The high energy density of the hydrogenated composite electrode at  $600 \text{ }^\circ\text{C}$  is calculated to be  $46.0 \text{ Wh kg}^{-1}$  at the high power density of  $21.8 \text{ kW kg}^{-1}$  (at  $50 \text{ A g}^{-1}$ ). Even at the low power density of  $0.5 \text{ kW kg}^{-1}$ , the energy density can reach as high

as  $81.5 \text{ Wh kg}^{-1}$ . However, as a comparison, the energy densities of the hydrogenated composite electrodes at  $800 \text{ }^\circ\text{C}$ ,  $400 \text{ }^\circ\text{C}$ , and the untreated composite electrode are presented to be  $33.1 \text{ Wh kg}^{-1}$  at  $20.6 \text{ kW kg}^{-1}$ ,  $25.8 \text{ Wh kg}^{-1}$  at  $20.5 \text{ kW kg}^{-1}$ , and  $15.5 \text{ Wh kg}^{-1}$  at  $19.2 \text{ kW kg}^{-1}$ , respectively, at the same current density of  $50 \text{ A g}^{-1}$ . Hence, the hydrogenated temperature plays an important role in the electrochemical performance of the  $\text{MnO}_2/\text{H-TiO}_2/\text{CMF NW}$  composite electrodes.

The EIS measurements of the  $\text{MnO}_2/\text{TiO}_2/\text{CMF NW}$  composite electrode and the  $\text{MnO}_2/\text{H-TiO}_2/\text{CMF NW}$  composite electrodes at  $400 \text{ }^\circ\text{C}$ ,  $600 \text{ }^\circ\text{C}$  and  $800 \text{ }^\circ\text{C}$  were conducted with  $5 \text{ mV}$  amplitude in a frequency range from  $0.01 \text{ Hz}$  to  $100 \text{ kHz}$ . Figure 5(f) shows the Nyquist plots of the different composite electrodes, and the inset is the magnified section in the high frequency. The plots consist of a compressed arc in the high-frequency range and a sloped line in the low-frequency region. The large slope of the vertical line in the low-frequency region is an indication of an ideal capacitive behavior mainly from the pseudocapacitance of  $\text{MnO}_2$  active materials.<sup>34</sup> And the approximately same slope suggests the same action of  $\text{MnO}_2$  in different composite electrodes. In the high-frequency region, both of the intercepts and smaller diameters of the arcs on the real axis of the hydrogenated composite electrodes are smaller than those of the untreated composite electrode, which indicates the smaller equivalent series resistance (ESR) and the smaller interfacial Faradic charge transfer resistance of the hydrogenated composite electrodes. Clearly, the  $\text{MnO}_2/\text{H-TiO}_2/\text{CMF NW}$

composite electrode at 600 °C shows the smallest ESR value (2.78 Ω) compared with others (2.94 Ω, 3.01 Ω and 3.41 Ω for the hydrogenated composite electrodes at 800 °C, 400 °C, and the untreated composite electrode, respectively), confirming that the non-linearly improving electrical conductivity is obtained with the hydrogenated temperature rising, and hence the MnO<sub>2</sub>/H-TiO<sub>2</sub>/CMF NW composite electrode at 600 °C exhibits the best electrochemical performance.

To quantitatively investigate the physical mechanism for improving the electrical conductivity of TiO<sub>2</sub> NWs after hydrogenation, the M-S plots of the TiO<sub>2</sub>/CMF NWs and the H-TiO<sub>2</sub>/CMF NWs at 400 °C, 600 °C and 800 °C were measured at the frequency of 10 Hz, as shown in Figure 6. As expected, all line sections of the plots exhibit a positive slope, indicating the n-type semiconductor feature. The space charge capacitance ( $C_s$ ) of a semiconductor is expressed using the following Eq. (6),<sup>35-37</sup> according to the M-S theory,

$$\frac{1}{C_s^2} = \frac{2}{\epsilon\epsilon_0 e_0 N_d} \left( U - U_{fb} - \frac{k_B T}{e_0} \right) \quad (6)$$

where  $C_s$  (F cm<sup>-2</sup>) is the space charge capacitance per unit area,  $N_d$  (cm<sup>-3</sup>) is the electron concentration,  $\epsilon$  is the dielectric constant (170 for rutile TiO<sub>2</sub>),<sup>38</sup>  $\epsilon_0$  (F m<sup>-1</sup>) is the permittivity of vacuum,  $e_0$  (C) is the electron charge,  $U$  (V) is the applied potential,  $U_{fb}$  (V) is the flat band potential,  $T$  (K) is the temperature, and  $k_B$  (J K<sup>-1</sup>) is the Boltzmann constant. From the Figure 6, the electron concentration of the H-TiO<sub>2</sub> NWs at 600 °C, 800 °C, 400 °C, and

TiO<sub>2</sub> NWs is obtained to be  $1.2 \times 10^{25} \text{ S}^{-2} \text{ cm}^{-3}$ ,  $7.7 \times 10^{24} \text{ S}^{-2} \text{ cm}^{-3}$ ,  $5.4 \times 10^{24} \text{ S}^{-2} \text{ cm}^{-3}$ ,  $2.2 \times 10^{24} \text{ S}^{-2} \text{ cm}^{-3}$ , respectively. It is noteworthy that the M-S Eq. (6) is derived from a planar electrode model. Thus, either the projected area for thin films or the specific surface area for the nanomaterials should be used in the calculation. Here, S represents the specific surface area of the TiO<sub>2</sub> NWs. All the samples are supposed to have the same S within the error. It is evident that the electron concentration of the H-TiO<sub>2</sub> NWs at 400 °C, 800 °C and 600 °C increases substantially in sequence, respectively, which is consistent with the results obtained from the EIS measurements. Their electron concentration is enhanced by about 2.5 times, 3.5 times, and 5.5 times compared with the untreated TiO<sub>2</sub> NWs, respectively. The M-S plots are also used to extrapolate  $U_{fb}$  of the different samples. It is about -0.57 V, -0.67 V, -0.69 V, and -0.76 V for TiO<sub>2</sub> NWs, H-TiO<sub>2</sub> NWs at 400 °C, 800 °C, and 600 °C, respectively. Hydrogenation causes negative shift of  $U_{fb}$ , i.e., the Fermi level of TiO<sub>2</sub> NWs should shift a corresponding absolute value of  $U_{fb}$  towards conduction band edge after the hydrogenation and the degree of up-shift for the H-TiO<sub>2</sub> NWs at 400 °C, 800 °C and 600 °C increases in sequence (the schematic diagram as shown in Figure S4). The up-shift of the Fermi level demonstrates the increase of the electron concentration and the improvement of the electrical conductivity in TiO<sub>2</sub> NWs. Based on these results, the MnO<sub>2</sub>/H-TiO<sub>2</sub>/CMF NW composite electrode at 600 °C with the best electrochemical properties can be related to the increase of the electrical conductivity, which is determined by the following Eq. (7),

$$\sigma = N_d e_0 \mu \quad (7)$$

Where  $\sigma$  (S cm<sup>-1</sup>),  $N_d$  (cm<sup>-3</sup>),  $e_0$  (C), and  $\mu$  (cm<sup>2</sup>V<sup>-1</sup>s<sup>-1</sup>) are the electrical conductivity, electron concentration, electron charge, and mobility of the electrode materials, respectively. The electrical conductivity of H-TiO<sub>2</sub> NWs at 400 °C, 800 °C, and 600 °C can be enhanced by about 2.5 times, 3.5 times, and 5.5 times compared with the untreated TiO<sub>2</sub> NWs, respectively. All the measurements were carried out at the same conditions except the hydrogenated temperature in order to rule out the effect of other factors. It is interesting to quantitatively investigate on how the electrical conductivity of the TiO<sub>2</sub> NWs is changed after the hydrogenation treatment. The formed H<sub>0</sub>, H<sub>i</sub>, or HO<sub>0</sub><sup>•</sup> defects during the hydrogenation could behave as shallow donors in TiO<sub>2</sub>. The HO<sub>0</sub><sup>•</sup> defects have the lowest formation energy over the whole Fermi level range under both oxidizing and reducing conditions by the density functional theory calculations.<sup>39</sup> As it is well understood that the higher the hydrogenated temperature is, the more the free electrons generated from the HO<sub>0</sub><sup>•</sup> defects become. In fact, the free electrons in TiO<sub>2</sub> NWs originate from the intrinsic defects (or oxygen vacancies) and the HO<sub>0</sub><sup>•</sup> defects. However, from the XRD analysis, the oxygen vacancies are significantly reduced via hydrogenation. From the data of the EIS spectra and M-S plots, the electron concentration of the hydrogenated composite electrodes becomes larger and the electrical conductivity is increased with the hydrogenated temperature rising until 600 °C, while the electron

concentration of the hydrogenated composite electrode at 800 °C becomes small and the electrical conductivity becomes low. We summarize that (i) the free electrons in TiO<sub>2</sub> NWs mainly originate from both of the oxygen vacancies and the HO<sub>o</sub><sup>•</sup> defects after hydrogenation. The electron concentration in TiO<sub>2</sub> NWs increases firstly until 600 °C and decreases later; (ii) the free electrons provided from the HO<sub>o</sub><sup>•</sup> defects are gradually increased with the hydrogenated temperature rising. The higher the hydrogenated temperature is, the more the amount of the HO<sub>o</sub><sup>•</sup> defects is, and the more the free electrons contributed are; (iii) it is proposed that the effect of the hydrogenation conditions on the crystalline perfection is very weak according to the little change of the FWHMs for the XRD peaks when the electrodes are hydrogenated at temperature between 400 °C and 600 °C, i.e., few oxygen vacancies are reduced. The enhancement of the free electrons in TiO<sub>2</sub> NWs could mainly result from the HO<sub>o</sub><sup>•</sup> defects. However, the crystalline quality is significantly improved at 800 °C. Much oxygen vacancies are reduced, which results in the decrease of the free electrons from the oxygen vacancies. While, at the hydrogenated temperature of 800 °C, the more hydrogen atoms doped into TiO<sub>2</sub> as shadow donors are, the more free electrons provided by them are. However, the electrical conductivity of the hydrogenated composite electrode at 800 °C is smaller than that of the hydrogenated composite electrode at 600 °C in terms of the M-S plots, indicating that the free electrons from the oxygen vacancies could

dominate the electrical conductivity, while these free electrons contributed from the  $\text{HO}_\circ$  defects could only have an assistant effect on the electrical conductivity.

Another important requirement for SC applications is the long-term cycling stability. The cycling life of the  $\text{MnO}_2/\text{H-TiO}_2/\text{CMF}$  NW composite electrode at  $600\text{ }^\circ\text{C}$  was evaluated by GCD test at the current density of  $10\text{ A g}^{-1}$  in the potential range of  $0\text{ V}$  to  $1.0\text{ V}$  for more than 5000 cycles, as shown in Figure 7. The electrode exhibits excellent stability with 90% retention of the initial capacitance after 5000 cycles and the last 10 cycles remain almost the same shape with the first 10 cycles (insets of Figure 7), illustrating the excellent long-term cycling stability of the composite electrode, especially compared with others, such as the  $\text{MnO}_2/\text{graphitic petal}/\text{carbon nanotube}$  composite electrode (nearly 90% after 1000 cycles at  $100\text{ mV s}^{-1}$ ),<sup>40</sup>  $\text{NiCo}_2\text{O}_4@\text{MnO}_2$  core-shell NW array electrode (88% after 2000 cycles at  $10\text{ mA cm}^{-2}$ ),<sup>41</sup>  $\text{MnO}_2/\text{C}/\text{TiO}_2$  shell/shell/core array electrode (78.7% after 1000 cycles at  $2\text{ A g}^{-1}$ ),<sup>42</sup> and  $\text{H-TiO}_2$  nanotube array electrode hydrogenated at  $600\text{ }^\circ\text{C}$  (74% after 10000 cycles at  $100\text{ mV s}^{-1}$ ).<sup>43</sup> From the results above, the hydrogenation at  $600\text{ }^\circ\text{C}$  can greatly enhance the electrochemical performance with the excellent cycling stability.

#### 4. Conclusions

In summary, we have quantitatively investigated the contribution of hydrogenation to the performance of  $\text{MnO}_2/\text{H-TiO}_2$  composite electrodes for

supercapacitor. The H-TiO<sub>2</sub> NWs hydrogenated at 600 °C provide high conductivity and facile ion transport. The electrical conductivity is determined by the carrier concentration in the materials. The electrical conductivity of electrode materials for supercapacitor plays an important role in the electrochemical performance. High capacitance and high cycling stability for MnO<sub>2</sub>/H-TiO<sub>2</sub> composite electrode hydrogenated at 600 °C are obtained. This work provides an idea for rationally designing the high-performance SCs and assembling novel nanostructures with preferable electrochemical performance.

### **Acknowledgments**

This work was partially supported by the Natural Science Foundation of China (No.51172058 and 51472066), the Key Project of Natural Science Foundation of Heilongjiang Province (ZD201112 and A201007), and Institution of Higher Education, Doctoral Fund Jointly Funded Project (20112329110001), and the Graduate Students' Scientific Research Innovation Project of Heilongjiang Province (HSDSSCX2014-05).

## Notes and References

- 1 W. F. Wei, X. W. Cui, W. X. Chen and D. G. Ivey, *Chem. Soc. Rev.*, 2011, **40**, 1697.
- 2 Q. Lu, J. G. Chen and J. Q. Xiao, *Angew. Chem. Int. Ed.*, 2013, **52**, 1882.
- 3 Q. Li, X. F. Lu, H. Xu, Y. X. Tong and G. R. Li, *ACS Appl. Mater. Interfaces*, 2014, **6**, 2726.
- 4 G. P. Wang, L. Zhang and J. J. Zhang, *Chem. Soc. Rev.*, 2012, **41**, 797.
- 5 P. Simon and Y. Gogotsi, *Nat. Mater.*, 2008, **7**, 845.
- 6 L. H. Bao, J. F. Zang and X. D. Li, *Nano Lett.*, 2011, **11**, 1215.
- 7 C. Liu, F. Li, L. P. Ma and H. M. Cheng, *Adv. Mater.*, 2010, **22**, E28.
- 8 Z. Chen, Y. C. Qin, D. Weng, Q. F. Xiao, Y. T. Peng, X. L. Wang, H. X. Li, F. Wei and Y. F. Lu, *Adv. Funct. Mater.*, 2009, **19**, 3420.
- 9 P. C. Chen, H. T. Chen, J. Qiu and C. W. Zhou, *Nano Res.*, 2010, **3**, 594.
- 10 J. W. Lee, T. Ahn, J. H. Kim, J. M. Ko and J. D. Kim, *Electrochim. Acta*, 2011, **56**, 4849.
- 11 X. C. Dong, H. Xu, X. W. Wang, Y. X. Huang, M. B. Chan-Park, H. Zhang, L. H. Wang, W. Huang and P. Chen, *ACS Nano*, 2012, **6**, 3206.
- 12 H. N. Zhang, Y. J. Chen, W. W. Wang, G. H. Zhang, M. Zhuo, H. M. Zhang, T. Yang, Q. H. Li and T. H. Wang, *J. Mater. Chem. A*, 2013, **1**, 8593.
- 13 Z. Chen, V. Augustyn, X. L. Jia, Q. F. Xiao, B. Dunn and Y. F. Lu, *ACS Nano*, 2012, **6**, 4319.

- 14 J. H. Kong, Y. F. Wei, C. Y. Zhao, M. Y. Toh, W. A. Yee, D. Zhou, S. L. Phua, Y. L. Dong and X. H. Lu, *Nanoscale*, 2014, **6**, 4352.
- 15 J. B. Wu, R. Q. Guo, X. H. Huang and Y. Lin, *J. Power Sources*, 2013, **243**, 317.
- 16 K. Xiao, J. W. Li, G. F. Chen, Z. Q. Liu, N. Li and Y. Z. Su, *Electrochim. Acta*, 2014, **149**, 341.
- 17 K. H. Ye, Z. Q. Liu, C. W. Xu, N. Li, Y. B. Chen, Y. Z. Su. *Inorg. Chem. Commun.*, 2013, **30**, 1.
- 18 J. P. Liu, J. Jiang, C. W. Cheng, H. X. Li, J. X. Zhang, H. Gong and H. J. Fan, *Adv. Mater.*, 2011, **23**, 2076.
- 19 L. Y. Yuan, X. H. Lu, X. Xiao, T. Zhai, J. J. Dai, F. C. Zhang, B. Hu, X. Wang, L. Gong, J. Chen, C. G. Hu, Y. X. Tong, J. Zhou and Z. L. Wang, *ACS Nano*, 2012, **6**, 656.
- 20 X. H. Lu, D. Z. Zheng, T. Zhai, Z. Q. Liu, Y. Y. Huang, S. L. Xie and Y. X. Tong, *Energy Environ. Sci.*, 2011, **4**, 2915.
- 21 Q. Yang, X. T. Zhang, M. Y. Zhang, Y. Gao, H. Gao, X. C. Liu, H. Liu, K. W. Wong and W. M. Lau, *J. Power Sources*, 2014, **272**, 654.
- 22 J. Yan, E. Khoo, A. Sumboja and P. S. Lee, *ACS Nano*, 2010, **4**, 4247.
- 23 T. Leshuk, R. Parviz, P. Everett, H. Krishnakumar, R. A. Varin and F. Gu, *ACS Appl. Mater. Interfaces*, 2013, **5**, 1892.
- 24 S. Murugesan, P. Kuppusami, N. Parvathavarthini and E. Mohandas, *Surf. Coat. Technol.*, 2007, **201**, 7713.

- 25 G. M. Wang, H. Y. Wang, Y. C. Ling, Y. C. Tang, X. Y. Yang, R. C. Fitzmorris, C. C. Wang, J. Z. Zhang and Y. Li, *Nano Lett.*, 2011, **11**, 3026.
- 26 X. H. Lu, M. H. Yu, G. M. Wang, T. Zhai, S. L. Xie, Y. C. Ling, Y. X. Tong and Y. Li, *Adv. Mater.*, 2013, **25**, 267.
- 27 H. Wu, C. Xu, J. Xu, L. F. Lu, Z. Y. Fan, X. Y. Chen, Y. Song and D. D. Li, *Nanotechnology*, 2013, **24**, 455401.
- 28 A. E. Fischer, K. A. Pettigrew, D. R. Rolison, R. M. Stroud and J. W. Long, *Nano Lett.*, 2007, **7**, 281.
- 29 X. B. Jin, W. Z. Zhou, S. W. Zhang and G. Z. Chen, *Small*, 2007, **3**, 1513.
- 30 A. Chaves, R. S. Katiyar and S. P. S. Porto, *Phys. Rev. B*, 1974, **10**, 1974.
- 31 O. Frank, M. Zukalova, B. Laskova, J. Kürti, J. Koltai and L. Kavan, *Phys. Chem. Chem. Phys.*, 2012, **14**, 14567.
- 32 K. R. Zhu, M. S. Zhang, Q. Chen, Z. Yin, *Phys. Lett. A*, 2005, **340**, 220.
- 33 J. C. Parker and R. W. Siegel, *Appl. Phys. Lett.*, 1990, **57**, 943.
- 34 J. G. Wang, Y. Yang, Z. H. Huang and F. Y. Kang, *J. Power Sources*, 2013, **224**, 86.
- 35 H. Tsuchiya, J. M. Macak, A. Ghicov, A. S. Rader, L. Taveira and P. Schmuki, *Corros. Sci.*, 2007, **49**, 203.
- 36 H. Zhou and Y. R. Zhang, *J. Phys. Chem. C*, 2014, **118**, 5626.
- 37 R. V. D. Krol, A. Goossens and J. Schoonman, *J. Electrochem. Soc.*, 1997, **144**, 1723.
- 38 R. A. Parker, *Phys. Rev.*, 1961, **124**, 1719.

- 39 T. S. Bjørheim, S. Stølen and T. Norby, *Phys. Chem. Chem. Phys.*, 2010, **12**, 6817.
- 40 G. P. Xiong, K. P. S. S. Hembram, R. G. Reifengerger and T. S. Fisher, *J. Power Sources*, 2013, **227**, 254.
- 41 L. Yu, G. Q. Zhang, C. Z. Yuan and X. W. Lou, *Chem. Commun.*, 2013, **49**, 137.
- 42 S. N. Yang, K. Cheng, J. C. Huang, K. Ye, Y. Xu, D. X. Cao, X. M. Zhang and G. L. Wang, *Electrochim. Acta*, 2014, **120**, 416.
- 43 X. H. Lu, G. M. Wang, T. Zhai, M. H. Yu, J. Y. Gan, Y. X. Tong and Y. Li, *Nano Lett.*, 2012, **12**, 1690.

## Figure Captions

Figure 1. (a and b) Typical low- and high-magnified SEM images of H-TiO<sub>2</sub>/CMF NWs at 600 °C. (c and d) Typical low- and high-magnified SEM images of the MnO<sub>2</sub>/H-TiO<sub>2</sub>/CMF NWs at 600 °C.

Figure 2. TEM images of (a) a bare H-TiO<sub>2</sub> NW at 600 °C and (b) a single MnO<sub>2</sub>/H-TiO<sub>2</sub> NW at 600 °C. (c) SAED pattern of the corresponding MnO<sub>2</sub>/H-TiO<sub>2</sub> NW. (d) High-resolution TEM image of the corresponding MnO<sub>2</sub>/H-TiO<sub>2</sub> NW. And the inset shows a magnified TEM image of the local area in the Figure 2(d). (e) The EDS line-scan spectra (indicated by the red line in the inset) of the MnO<sub>2</sub>/H-TiO<sub>2</sub> NW.

Figure 3. (a) The XRD patterns of TiO<sub>2</sub>/CMF NWs and H-TiO<sub>2</sub>/CMF NWs hydrogenated at different temperatures. (b) The Raman spectra of TiO<sub>2</sub>/CMF NWs and H-TiO<sub>2</sub>/CMF NWs hydrogenated at different temperatures.

Figure 4. (a) The CV curves of MnO<sub>2</sub>/TiO<sub>2</sub>/CMF NW composite electrode, TiO<sub>2</sub>/CMF NW electrode, and MnO<sub>2</sub>/CMF electrode at the scan rate of 10 mV s<sup>-1</sup>. (b) The GCD curves of MnO<sub>2</sub>/TiO<sub>2</sub>/CMF NW composite electrode, TiO<sub>2</sub>/CMF NW electrode, and MnO<sub>2</sub>/CMF electrode at the current density of 10 A g<sup>-1</sup>. (c) The CV curves of MnO<sub>2</sub>/TiO<sub>2</sub>/CMF NW composite electrode at various scan rates. (d) The GCD curves of MnO<sub>2</sub>/TiO<sub>2</sub>/CMF NW composite electrode at various current densities.

Figure 5. (a) The CV curves of MnO<sub>2</sub>/TiO<sub>2</sub>/CMF NW composite electrode and MnO<sub>2</sub>/H-TiO<sub>2</sub>/CMF NW composite electrodes at 400 °C, 600 °C and

800 °C at 10 mV s<sup>-1</sup>. (b) The specific capacitance of the different composite electrodes as a function of the scan rate. (c) The GCD curves of MnO<sub>2</sub>/TiO<sub>2</sub>/CMF NW composite electrode and MnO<sub>2</sub>/H-TiO<sub>2</sub>/CMF NW composite electrodes at 400 °C, 600 °C and 800 °C at 10 A g<sup>-1</sup>. (d) The specific capacitance of the different composite electrodes as a function of the current density. (e) The Ragon plots of MnO<sub>2</sub>/TiO<sub>2</sub>/CMF NW composite electrode and MnO<sub>2</sub>/H-TiO<sub>2</sub>/CMF NW composite electrodes at 400 °C, 600 °C and 800 °C. (f) The Nyquist plots of MnO<sub>2</sub>/TiO<sub>2</sub>/CMF NW composite electrode and MnO<sub>2</sub>/H-TiO<sub>2</sub>/CMF NW composite electrodes at 400 °C, 600 °C and 800 °C. The inset is the corresponding magnified section within the high frequency.

Figure 6. The M-S plots of TiO<sub>2</sub>/CMF NW electrode and H-TiO<sub>2</sub>/CMF NW electrodes at 400 °C, 600 °C and 800 °C.

Figure 7. The specific capacitance retention of MnO<sub>2</sub>/H-TiO<sub>2</sub>/CMF NW composite electrode at 600 °C as a function of cycle numbers, and the insets are the GCD curves of first 10 cycles and last 10 cycles, respectively.

**Table caption**

Table I. FWHMs of diffraction peaks for untreated TiO<sub>2</sub> NWs and H-TiO<sub>2</sub> NWs at 400 °C, 600 °C and 800 °C.

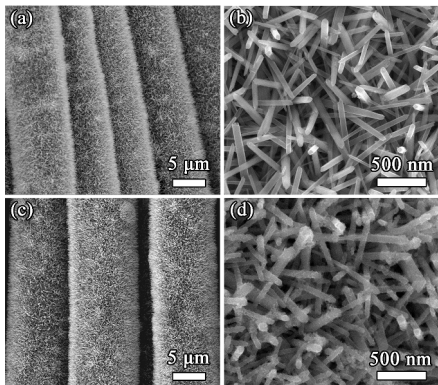


Figure 1 by X. Y. Cao, et al.

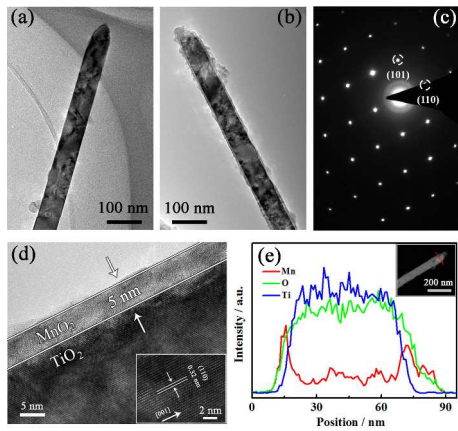


Figure 2 by X. Y. Cao, et al.

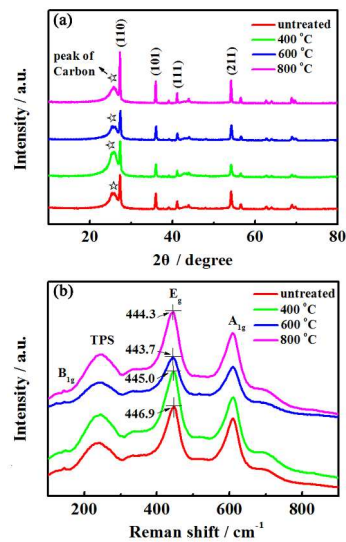


Figure 3 by X. Y. Cao, et al.

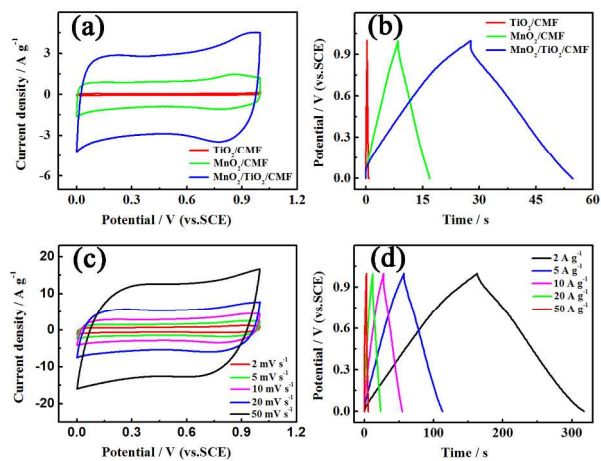


Figure 4 by X. Y. Cao, et al.

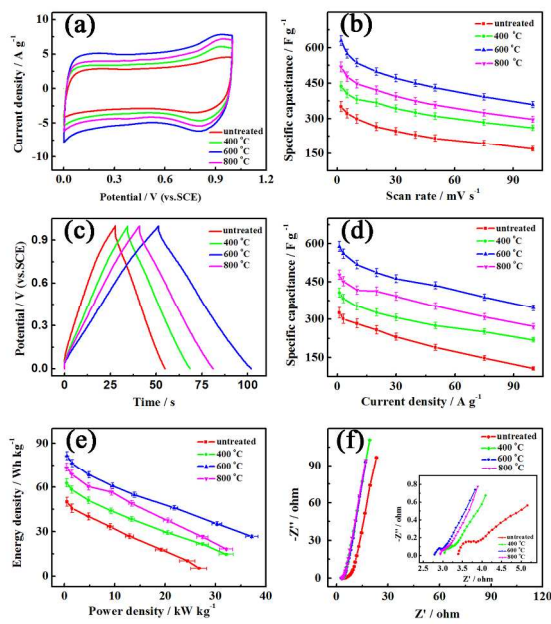


Figure 5 by X. Y. Cao, et al.

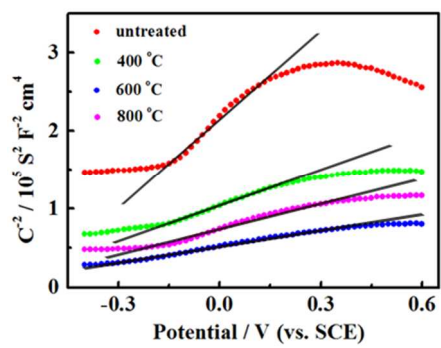


Figure 6 by X. Y. Cao, et al.

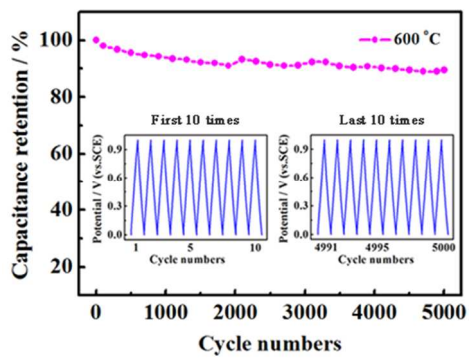


Figure 7 by X. Y. Cao, et al.

Table I by X. Y. Cao, et al.

TiO <sub>2</sub> NWs	FWHMs of XRD peaks		
	(110)	(101)	(211)
untreated	0.38	0.27	0.35
400 °C	0.37	0.25	0.34
600 °C	0.35	0.26	0.33
800 °C	0.22	0.19	0.23

# Quantitative investigation on hydrogenation to the performance of $\text{MnO}_2/\text{H-TiO}_2$ composite electrodes for supercapacitor

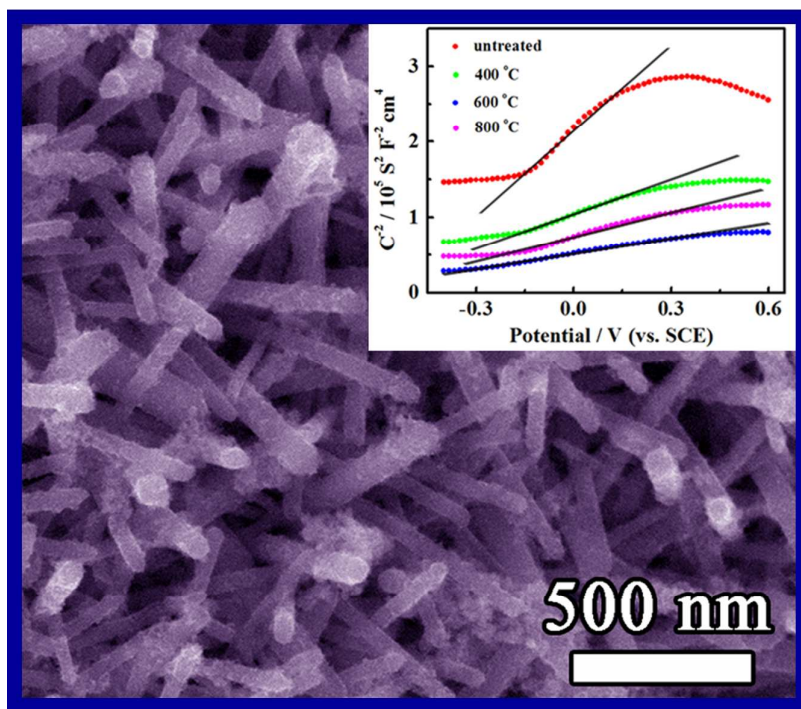
X. Y. Cao,<sup>a</sup> X. Xing,<sup>c</sup> N. Zhang,<sup>b</sup> H. Gao,<sup>a</sup> M. Y. Zhang,<sup>1,a</sup> and Y. C Shang,<sup>c</sup> X. T. Zhang,<sup>\*,a</sup>

<sup>a</sup> Key Laboratory for Photonic and Electronic Bandgap Materials, Ministry of Education, School of Physics and Electronic Engineering, Harbin Normal University, Harbin 150025, P. R. China.

<sup>b</sup> Department of Chemistry and Chemical Biology, Cornell University, Ithaca, USA.

<sup>c</sup> College of Chemistry and Chemical Engineering, Harbin Normal University, Harbin 150025, P. R. China.

## Graphical abstract



Based on the Mott-Schottky theory, the electron concentration of the as-synthesized nanostructures can be calculated by M-S plot.

<sup>1</sup>Corresponding author emails: [mystci@foxmail.com](mailto:mystci@foxmail.com), [xtzhangzhang@hotmail.com](mailto:xtzhangzhang@hotmail.com)